Flexible scintillator autoradiography for tumor margin inspection using < sup>18</sup>F-FDG

K. N. Vyas, M. Grootendorst, T. Mertzanidou, S. Macholl, D. Stoyanov, et al.

K. N. Vyas, M. Grootendorst, T. Mertzanidou, S. Macholl, D. Stoyanov, S. R. Arridge, D. S. Tuch, "Flexible scintillator autoradiography for tumor margin inspection using ¹⁸F-FDG," Proc. SPIE 10478, Molecular-Guided Surgery: Molecules, Devices, and Applications IV, 1047811 (1 March 2018); doi: 10.1117/12.2289693

SPIE.

Event: SPIE BiOS, 2018, San Francisco, California, United States

Flexible scintillator autoradiography for tumor margin inspection using ^{18}F-FDG

K. N. Vyas*[a], M. Grootendorst [a], T. Mertzanidou [b], S. Macholl [c], D. Stoyanov [b], S. R. Arridge [b], D. S. Tuch [a]

[a]Lightpoint Medical Ltd, Misbourne Works, Waterside, Chesham, HP5 1PE, United Kingdom; [b]Centre for Medical Image Computing, University College London, Gower St, Bloomsbury, London WC1E 6BT, United Kingdom; [c]Invicro, Barts Cancer Institute, Queen Mary University of London, United Kingdom; *kunal.vyas@lightpointmedical.com; phone +44 (0) 1494 917 697

ABSTRACT

Autoradiography potentially offers high molecular sensitivity and spatial resolution for tumor margin estimation. However, conventional autoradiography requires sectioning the sample which is destructive and labor-intensive. Here we describe a novel autoradiography technique that uses a flexible ultra-thin scintillator which conforms to the sample surface. Imaging with the flexible scintillator enables direct, high-resolution and high-sensitivity imaging of beta particle emissions from targeted radiotracers. The technique has the potential to identify positive tumor margins in fresh unsectioned samples during surgery, eliminating the processing time demands of conventional autoradiography. We demonstrate the feasibility of the flexible autoradiography approach to directly image the beta emissions from radiopharmaceuticals using lab experiments and GEANT-4 simulations to determine i) the specificity for ^{18}F compared to ^{99m}Tc-labeled tracers ii) the sensitivity to detect signal from various depths within the tissue. We found that an image resolution of 1.5 mm was achievable with a scattering background and we estimate a minimum detectable activity concentration of 0.9 kBq/ml for ^{18}F. We show that the flexible autoradiography approach has high potential as a technique for molecular imaging of tumor margins using ^{18}F-FDG in a tumor xenograft mouse model imaged with a radiation-shielded EMCCD camera. Due to the advantage of conforming to the specimen, the flexible scintillator showed significantly better image quality in terms of tumor signal to whole-body background noise compared to rigid and optimally thick CaF_2:Eu and BC400. The sensitivity of the technique means it is suitable for clinical translation.

Keywords: 18F-FDG, Surgical imaging, Flexible scintillator, Tumor margin assessment, Breast Cancer, Molecular imaging

1. INTRODUCTION

Surgical intervention is often a necessary and primary means of treatment for localized cancer tumors. It is often important the excision is made precisely ensuring all the cancerous mass is removed whilst viable healthy tissue is retained to provide the best outcome for the patient. There is a tension between not removing enough tissue thereby increasing the risk of reoccurrence, and removing too much tissue thereby adversely affecting physiological function. Tumor margin assessment is therefore crucial in determining the success of a surgical oncology procedure. In particular, if cancerous cells are found on the surface of an excision during assessment of the surgical margin, further treatment including reoperation may be necessary.

Margin assessment in the clinic is conventionally done postoperatively using histopathological staining. Emerging interoperative imaging technologies, such as Cerenkov Luminescence Imaging (CLI) [1] and targeted fluorescence imaging [2] are being developed to allow surgeons to estimate the margin status during surgery and therefore immediately act on their findings, for example by removing more tissue, with the aim to improve patient outcomes and reduce reoperation rates. The success of these technologies depends on the sensitivity, which is related to the signal to noise achievable, as well as the availability of molecular probes with sufficient specificity.

Autoradiography offers high molecular sensitivity and spatial resolution [3] and could, therefore, provide a potential technique for interoperative tumor margin estimation. However, conventional autoradiography requires sectioning the sample which destroys the specimen and which is labor-intensive. Instead we propose to simplify the process by using a

Molecular-Guided Surgery: Molecules, Devices, and Applications IV, edited by Brian W. Pogue, Sylvain Gioux,
Proc. of SPIE Vol. 10478, 1047811 · © 2018 SPIE · CCC code: 1605-7422/18/$18 · doi: 10.1117/12.2289693

flexible ultra-thin scintillator which conforms to the sample surface and thus obviates tissue sectioning. One major advantage of the technique is that it can be used with clinically-approved radiopharmaceuticals [4].

In this work we report simulations as well as lab based measurements to benchmark the performance of the flexible scintillator with the rigid alternatives of CaF_2:Eu and BC400 scintillators. These scintillators were chosen due to their relatively low densities and Z numbers. For this application, it is important that the scintillators preferentially detect the beta particles originating from Positron Emission Tomography (PET) nuclide decay and that these scintillators are less sensitive to the gamma radiation that is produced from subsequent annihilation of positrons. The gamma radiation is usually measured in PET, but for the autoradiography technique presented here, this represents a source of background noise. As well as measuring the specificity for ^{18}F compared to measurements with ^{99m}Tc, a gamma emitter, we used simulations to report the depth of sensitivity of the signal.

Finally, we report our initial findings from our recent preclinical work showing that the flexible autoradiography approach has potential as a technique for molecular imaging of tumor margins. ^{18}F-fluorodeoxyglucose (^{18}F-FDG) was used in a triple negative breast cancer mouse model (MDA-MB-231 xenograft) and imaged with a radiation-shielded EMCCD camera. We intend to publish the full method and results of the preclinical study in a follow up peer reviewed publication.

2. METHODS

2.1 Materials

The scintillators used for the testing and considered for the modelling were 1000 μm thick CaF_2:Eu (herein referred to as CaF_2), 2000 μm thick BC400 and a 6 μm thick flexible scintillator. The BC400 and CaF_2 thickness were respectively chosen to approximately match the penetration depths of ^{18}F beta particles in these materials estimates using the NIST ESTAR stopping-power and range tables for electrons [5]. We are currently seeking permission from our manufacturing partner to disclose further details regarding the material and construction of the flexible scintillator and we aim to publish these in a follow up publication.

The GEANT-4 toolkit [6] was used for simulation of the scintillators and verifying their depth sensitivity. The GEANT-4 results were analyzed using MATLAB [7].

For the lab testing and preclinical work, the scintillators were imaged with the LightPath™ imaging system provided by Lightpoint Medical Ltd [8]. This consists of a tungsten-shielded camera with an electron multiplying charge coupled device (EMCCD) [9] sensor Peltier-cooled to -80 °C. The tungsten shielding minimizes interference due to direct radiation strikes on the sensor. The EMCCD has 512 x 512 pixels, each of size:16 x 16 μm. This is fitted with an f/0.95 lens with +2 diopter close-up with a Field of View (FOV) of 6 x 6 cm, giving an intrinsic spatial resolution of 117 μm and effective spatial resolution of 3.17 lp/mm; 158 μm. To obtain a spatial reference image, a high-resolution camera (1600 x 1200 pixels, 4.4 x 4.4 μm pixels) with a FOV that encompassed the FOV of the EMCCD was used. The EMCCD images were analyzed in MATLAB.

Table 1 shows the EMCCD settings used for the experiments.

EMCCD settings			
Parameter	*Value*	*Units*	*Comment*
Camera temperature	-80	°C	None
Pixel readout time	1	μs	1 MHz horizontal readout speed
Exposure time	10-300	s	Varies by experiment
EM gain	300	-	None
Vertical shift clock	3.3	μs	Default
Vertical clock voltage	Normal	-	Default
Pre-amp gain	3	-	Maximum
Horizontal binning	1	-	None
Vertical binning	1	-	None
Electron sensitivity	4.23	e- / ADU	None

Radioactive sources: ^{18}F and ^{99m}Tc solutions were used for the lab experiments, ^{18}F-FDG was used for the xenograft mouse model. Where activity or activity concentration is stated or used in a calculation it is always time-corrected for the time of imaging unless explicitly stated otherwise (e.g. injected dose).

2.2 Sensitivity and detection limit

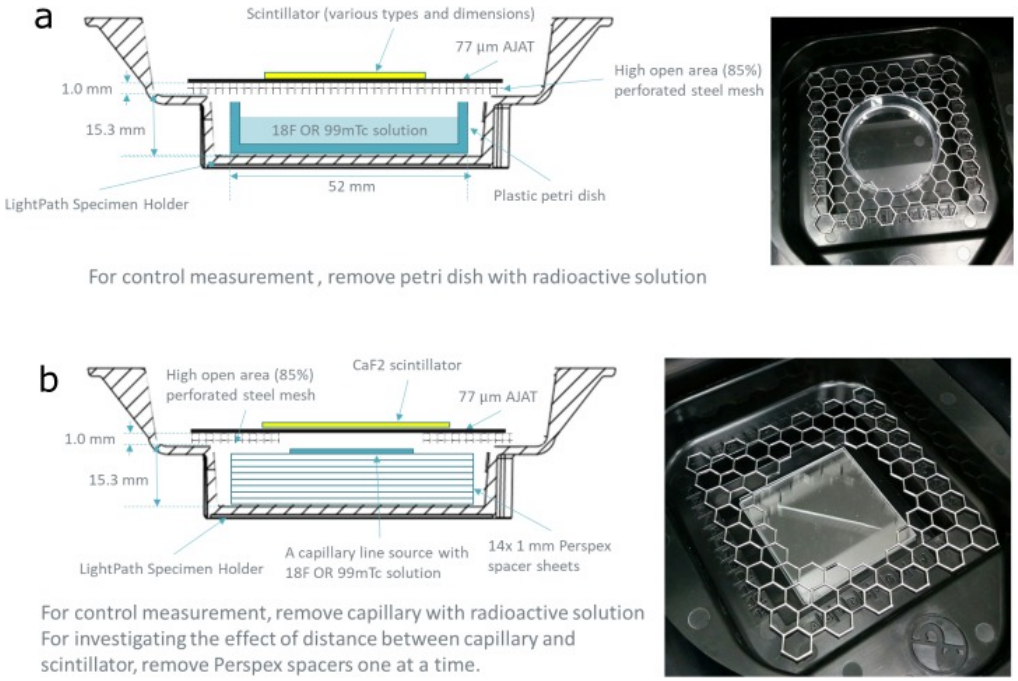

Figure 1. a) Diagram of the setup used for sensitivity experiments. The photo on the right shows the setup without the AJAT metalized polyvinyl chloride (m-PVC) film and scintillator to allow visibility of the source. b) Diagram showing the setup used for resolution experiments. The photo on the right shows the setup without the AJAT m-PVC and scintillator to allow visibility of the source. The glass capillary (Nominal ID 0.56 mm, OD 0.80 mm) was filled with approx. 1 MBq of fluorine 18 solution.

The setup shown in Figure 1(a) was used to measure the sensitivity of the scintillators to ^{18}F and ^{99m}Tc activity. A petri dish was filled with 4 ml of radioactive solution of known activity concentration and a scintillator was suspended above this at a fixed distance using a high open area mesh. The mesh is entirely open above the petri dish. A t = 10 s exposure time image was taken and the mean signal (m) in native analogue to digital units (ADU) per pixel per s was found for a region of interest within the footprint of the petri-dish and scintillator.

The offset and background signal are extracted from the signal intensity c_i in two control images (without activity present) taken with exposure times t_1 = 10 s and t_2 = 300 s as follows:

$$\mathrm{BG} = \frac{c_2 - c_1}{t_2 - t_1} \tag{1}$$

$$\mathrm{Offset} = c_2 - BG \cdot t_2 \tag{2}$$

where c_1 and c_2 are the mean ADU per pixel measured in the control images acquired with the same setup as images of radioactive samples, and using a region of interest of same size and position as those drawn on radioactive sample

images. The sensitivity (s) in ADU pixel^{-1} s^{-1} kBq^{-1} ml, is then calculated from images of radioactive samples with the mean signal (m) and image exposure time t as follows:

$$s = \frac{m - Offset - BG \cdot t}{t \cdot a(t)} \tag{3}$$

where $a(t)$ is the activity concentration of the radioactive sample in kBq ml^{-1} at the time of image acquisition.

We define the detection limit (d) as the point when the signal level equals the standard deviation (σ) of the noise (SNR=1). This is calculated for given camera settings as follows:

$$d = \frac{\sigma}{s \cdot t \cdot b^2} \tag{4}$$

where, σ is the measured standard deviation (noise) at the camera settings of interest, t is the exposure time and b is the binning applied, e.g. b=2 means each binned pixel is composed of 2x2 native pixels.

2.3 Specificity

The ^{18}F/^{99m}Tc specificity is found by taking the ratio of the sensitivities for ^{18}F and ^{99m}Tc.

Additionally, the proportion of the signal due to annihilation gammas for ^{18}F and gamma emissions for ^{99m}Tc is measuring with the addition of 5 mm poly(methyl methacrylate) (PMMA) between the scintillator and the source in the setup depicted in Figure 1(a) in order to attenuate all the charged particle emissions from the source. The remaining component of signal for ^{99m}Tc is due to shell electrons that are emitted for 10.7% of disintegrations due to internal conversion.

2.4 Resolution

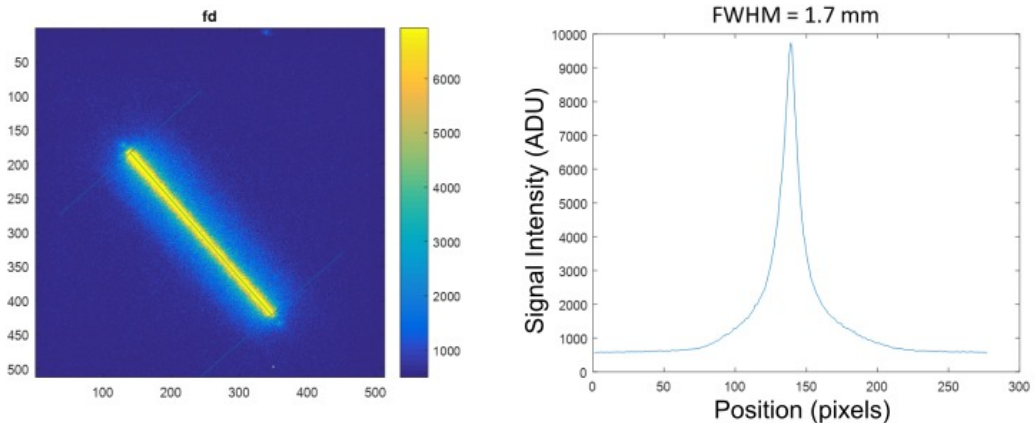

Figure 2. On the left is an example of an EMCCD image of the capillary seen using a flexible scintillator with the scintillator in contact with the capillary. The guideline along the length of the signal indicates the position of the capillary, the two guidelines normal to the capillary at either end indicate the direction in which the signal profiles are taken. These are taken along the length of the capillary with a spacing of 1 pixel and are then averaged. The resulting smooth response is shown in the graph on the right.

The setup described in Figure 1(b) was used to investigate the effect of distance between the source and the scintillator on resolution. A capillary filled with a high-activity concentration solution to make a line source. This was placed on a stack of PMMA spacers to provide a scattering background so that a realistic resolution is obtained. The scintillator was suspended above this using a high open area mesh. The capillary was placed at an angle in the field of view to reduce pixilation effects in the analysis.

Direct radiation strikes on the image sensor are easily excluded due to their extremely high intensity compared other parts of the image. The capillary position and slope are measured and multiple profiles are taken, normal to the capillary,

using bicubic interpolation to allow for profiles to be taken at diagonally across pixels. These profiles are averaged to obtain a smooth response function as depicted in Figure 2.

The intrinsic resolution (R) is estimated from the FWHM of the response function by adjusting for the finite OD of the capillary using the following relation:

$$R = \sqrt{FWHM^2 - OD^2} \tag{5}$$

2.5 Depth sensitivity

An extended ^{18}F source in tissue was simulated using GEANT4. All three scintillators were modelled using the inbuilt materials library. A 40 mm x 40 mm x 40 mm cube of normal density breast tissue (0.96) (50% fibrous/glandular, 50% adipose) [10,11] was simulated directly under the scintillator. The 64 ml volume of the tissue is consistent with reported wide local excision sizes [12,13]. Within the tissue a 10 mm long, 15 mm diameter cylindrical ^{18}F source was simulated. The ^{18}F positron emission energy probability distribution was used to simulate a realistic spectrum and the beta particles were allowed to scatter in the tissue and scintillator. Annihilations and the resulting 511 keV gamma emissions were also included [14].

The location of the source within the tissue was varied from touching the scintillator-tissue interface (depth = 0) down to being obscured by 10 mm of tissue (depth = 10 mm). For each setup, over 100,000 disintegrations we simulated. Scintillation photons in the visible spectrum (300 nm -1000 nm) were generated when the radiation interacted with the scintillator and these photons were recorded as signal if the exited the simulation through the top surface of the scintillator (away from the tissue). Signal due to beta particle interactions and gamma particle interactions were recorded separately, allowing us to plot the depth dependency of each independently.

In future work a forward model may be constructed if particle energy information is gathered, allowing for high resolution depth information to be reconstructed. This may work similarly to how wavelength dependent forward models can be constructed for CLI [15].

2.6 Image quality comparison for rigid and flexible scintillators

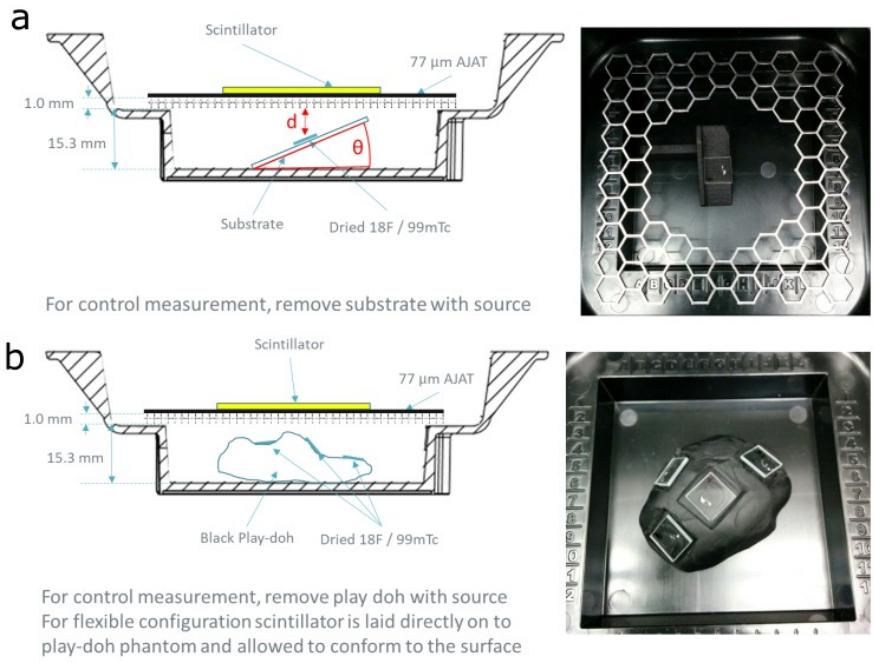

Figure 3. a) Diagram of the setup used to investigate how the angle and distance of an activity source from the scintillator changes the image obtained using a rigid scintillator. The photo on the right shows the setup without the AJAT and scintillator to allow visibility of the source. A dried source is placed on various 3D printed wedges to create setups with varying distance and angle. b) Diagram of the setup used to compare the flexible and rigid scintillator configurations using a phantom clinical sample made with playdoh. The diagram shows the rigid configuration and the photo on the right shows the playdoh phantom and arranged dried sources. For the flexible configuration, the scintillator is placed directly over this and allowed to conform to the sample for the rigid configuration the mesh and AJAT are first added.

To assess the change in image quality due to flexibility, independent of the scintillators chosen, the flexible scintillator was used in both a rigid and flexible configuration to measure simulated a playdoh phantom and dried ^{18}F sources arranged to mimic a clinical breast resection sample, see Figure 3(b). The image distortions seen in the rigid configuration due to source angle and distance are also systematically observed using 3D printed wedges, which are used to hold dried ^{18}F sources.

2.7 Preclinical mouse model

All animal studies were ethically reviewed and carried out in accordance with the UK Animals (Scientific Procedures) Act 1986 and were performed in accordance with British Home Office regulations governing animal experimentation. Measurements from eight female athymic nude mice (NU(NCr), homozygous) [16] were taken for the study, bearing a total of 16 human MDA-MB-231 subcutaneous tumor xenografts (one on each flank). Cells had been purchased from the American Tissue Culture Collection (ATCC code HTB-26™) and cultured as per the ATCC protocol [17]. Each mouse then received one subcutaneous injection on each flank with a mixture of 0.05 ml Matrigel and 0.05 ml suspension of 5 million MDA-MB-231 cells in phosphate buffer solution. The tumors were allowed to develop for 4 weeks.

For the experiment, each mouse was fasted for at least 4.5 hours, and then anaesthetized by isoflurane. A blood sample was taken from a lateral tail vein ca. 1-2 min before radiotracer injection to obtain an instant measurement of the blood glucose level by a commercial glucose monitor (Accu Chek). Ca. 20 MBq ^{18}F-FDG in 0.2 ml was injected into the other lateral tail vein. The accurate amount of injected activity was calculated from the difference of loaded syringe and emptied syringe with decay corrections to the time of injection. The animal was kept under general anesthesia (respiration rate around 40 to 60 breaths per minute) in a heat box set to 38 °C. After ca. 20 min, the animal was transferred to the PET/CT scanner (Inveon, Siemens) with continued isoflurane anesthesia and body heating via an electric heat mat. A whole-body CT scan was acquired and the CT image reconstructed. A whole-body PET scan was acquired from 40 to 50 min post radiotracer injection. This was reconstructed first by filtered back projection (FBP) as quality control (visual confirmation of ^{18}F signal in tumor), and later by ordered subset expectation maximization (OSEM) [18] for quantification. The animal was then sacrificed by CO_2 overdose and the skin between the upper and the lower legs was removed, exposing the tumors. Where possible, tumors were kept in their original position.

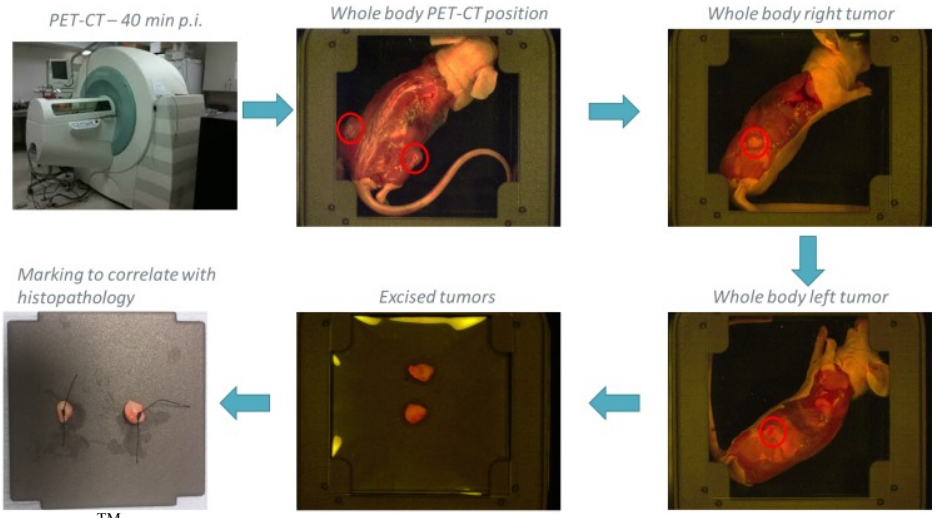

Figure 4. The LightPath™ system was used to take autoradiography images of the mouse. Several mice were imaged in the same position as in the PET-CT scan (whole body PET-CT position, prone), and all the mice were imaged in both sagittal orientations (whole body right and whole body left positions). Finally the excised tumors were imaged in isolation.

The LightPath™ system was used to take autoradiography images of the sacrificed mouse with the BC400, CaF_2 and flexible scintillators in various configurations, see Fig. 4. For each acquisition three 20 s frames were taken. To exclude

any stochastic noise due to direct radiation strikes on the sensor, the three frames were combined using a spatiotemporal median of 3 x 3 x 3 pixels.

Finally, the tumors were excised, weighed and imaged separately as depicted in Figure 4. For all the animal positions, images were taken with the BC400, CaF_2 and flexible scintillators with a stretched 50 µm polyester (PE) film between the mouse and the scintillator. The rigid scintillators were suspended 1 mm above the nominal position of the polyester film to avoid stress due to the bulge in the film caused by the mouse/tumors. Additionally, for the whole-body PET-CT position (prone), images were taken with the flexible scintillator conforming to the mouse, both with and without a 10 µm polyvinyl chloride (PVC) film in between.

The excised tumor images were used to measure the ratio of tumor signal to background noise for each scintillator. The whole body left and right images were used to measure the ratio of tumor signal to healthy-tissue background noise for each scintillator. The whole-body conforming images were used to verify that the flexible scintillators can image the tumor sources when they bend around the curve of the specimen and to compare the resulting surface weighted autoradiography measurement with the volumetric PET-CT scan.

A second radioactivity uptake measurement was performed on the excised tumors by gamma counting after conclusion of the autoradiography experiments. This may provide more accurate radioactivity quantification than PET-CT, albeit only on the whole tumors. Finally, tumor tissue sections at select depths of the tumor were haematoxylin and eosin (H&E) stained and then scanned.

3. RESULTS AND DISCUSSION

3.1 Depth sensitivity of scintillators

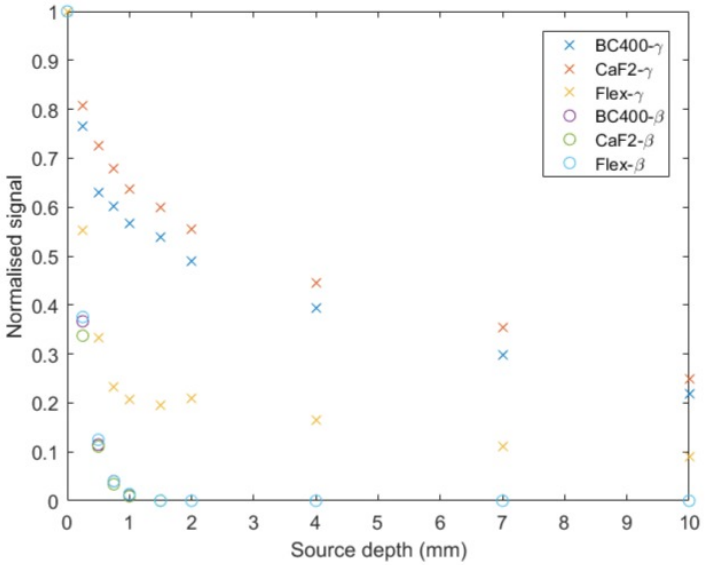

Figure 5. Simulations of BC400, CaF2 and flexible scintillators with GEANT4 showing how the signal from 18F beta particles (circles) and secondary gamma particles (crosses) from an extended source (10 mm long 15 mm diameter cylinder) decays with depth in the tissue. The signal has been normalized to be 1 for a superficial source (i.e. d = 0 mm).

Basic simulations conducted in GEANT4 show that the beta signal is limited to the first mm of tissue. As expected the sensitivity to the secondary 511 keV gammas drops off more slowly with tissue depth. The simulation results imply that the thin flexible scintillator is less sensitive to deeper gamma sources compared to superficial ones and is in this sense preferable to the thicker rigid alternatives. Note that the measured specificity of the flexible scintillator to betas was comparable to that of CaF_2 as reported below.

3.2 Relative sensitivity of scintillators

Table 2 shows the sensitivity for each scintillator measured for ^{18}F and ^{99m}Tc solution using the petri-dish setup shown in Figure 1(a).

Sensitivity (ADU pixel^{-1} s^{-1} kBq^{-1} ml)			
Scintillator	*^{18}F*	*^{99m}Tc*	*Specificity (^{18}F/^{99m}Tc)*
CaF_2	0.230	0.016	14.4
BC400	0.089	0.002	44.5
Flexible	0.051	0.004	12.8

Table 3 shows the predicted SNR=1 detection limits for a 10 s exposure time and native pixels (no binning) calculated using the sensitivity reported in Table 1 and a control background noise measurement for ^{18}F and ^{99m}Tc solution using the petri-dish setup shown in Figure 1(a).

Detection limit for a 10 s exposure time (kBq ml^{-1})			Detection limit for a 300 s exposure time and 8x8 binning (kBq ml^{-1})	
Scintillator	*^{18}F*	*^{99m}Tc*	*^{18}F*	*^{99m}Tc*
CaF2	5.6	82.6	0.1	1.9
BC400	15.0	753.3	0.3	17.2
Flexible	38.2	481.7	0.9	11.0

The measured sensitivity and predicted minimum detectable limit are presented in Table 2 and Table 3 respectively and show that as expected the rigid scintillators with optimal thickness outperform the flexible scintillator when compared with a fixed geometry (see Figure 1a). The CaF_2 offers the best sensitivity and lowest detection limit. All three scintillators showed good specificity (>10) for ^{18}F over the ^{99m}Tc (a possible interference in surgery) and BC400 was the most specific due to its lower density and Z numbers.

It was found that 4% of the ^{18}F signal was due to annihilation gammas and greater than 36% of the ^{99m}Tc signal was due to gamma emission from the isotope as measured with the flexible scintillator and a PMMA barrier to block the ^{18}F betas and ^{99m}Tc internal conversion electrons respectively.

3.3 Rigid versus flexible geometry

Real specimens are not homogenous or flat and therefore a more realistic comparison is required to ascertain if the flexible scintillator can overcome its shortcomings due to preferred geometry.

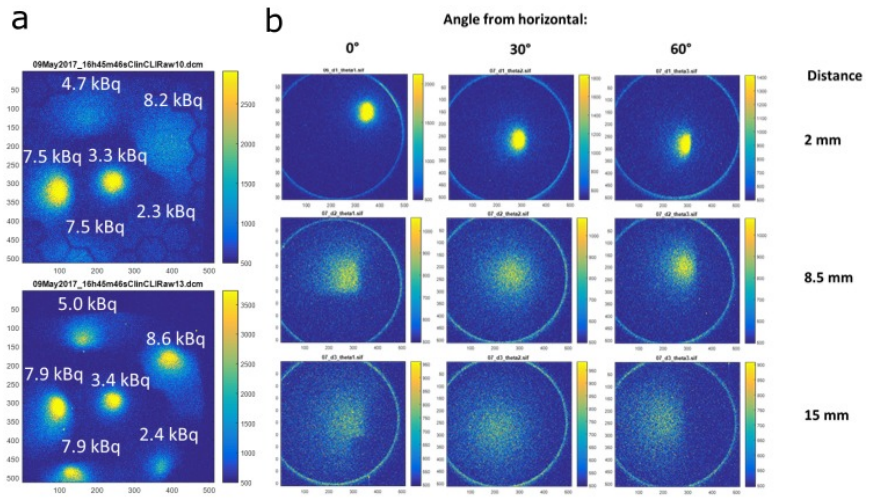

Figure 6. a) Images of a breast resection mimicking phantom with six dried 18F sources on the surface (see Figure 3(b)) taken with the flexible scintillator in a rigid configuration (top) and in a flexible configuration, where it could conform to the surface of the phantom (bottom). b) Images of dried ^{18}F sources mounted on wedges (see Figure 3(a)) demonstrating the spatial distortion due to angle and the loss of resolution and signal due to distance when using the rigid configuration.

Figure 6 shows the results of a qualitative comparison of the rigid and flexible configurations. In the rigid configuration, it can be seen that sources that are not at the apex of the phantom source suffer both a reduction in signal with increasing distance and spatial distortion due to the angle between the surface and the scintillator. Where the flexible scintillator could conform to the phantom surface the image quality is maintained across the field of view.

Table 4 shows the FWHM at d = 0.4 mm from the center of the capillary for a scattering background measured using the capillary setup described in section 2.3. The resolution is calculated using equation 5.

Measured FWHM and Resolution (mm)		
Scintillator	*FWHM*	*Resolution*
CaF_2	1.5 ± 0.1	1.3 ± 0.1
Flexible	1.7 ± 0.1	1.5 ± 0.1

The resolution measured with a scattering background, is similar for the 1000 μm thick rigid CaF_2 and the 6 μm thick flexible scintillator despite the large difference in thickness. This is because the resolution at the surface is limited by the beta particle scattering in the source and the light scatter in the scintillator.

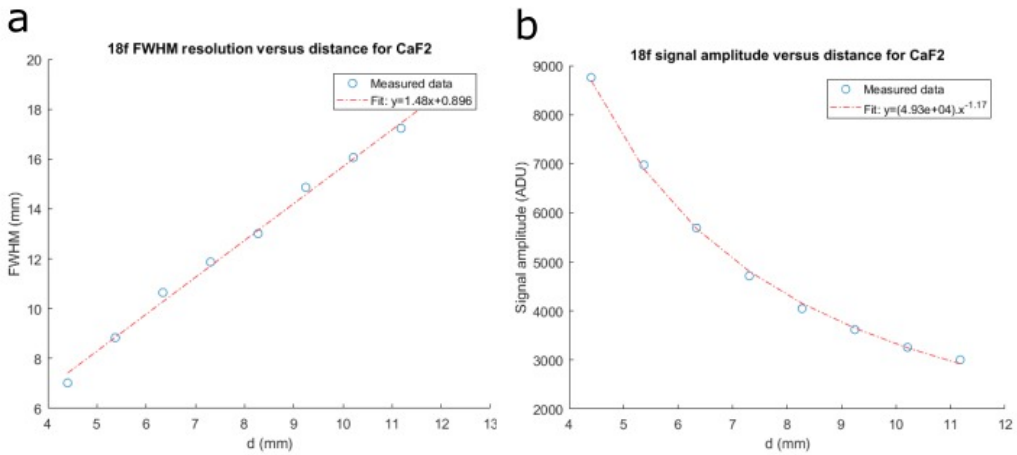

Figure 7. Using the capillary setup described in section 2.3 the FWHM (a) and the signal amplitude (b) were extracted from the profiles measured when varying the normal distance from the CaF_2 scintillator surface and the capillary, which was filled with F18 solution. The data points were further fitted with trend lines to reveal that the FWHM depends linearly on distance with a linear coefficient of 1.48 and the signal amplitude has a dependence of $d^{-1.17}$, close to the theoretical limit of d^{-1} for an infinitely long line source.

As clinically relevant irregular specimens are considered source to rigid scintillator distances greater than 1 mm need to be considered. Figure 6 shows that in this case the flexible scintillator becomes more favorable. The resolution drops off linearly with the distance and the 4.5x sensitivity advantage of the CaF_2 is quickly lost as the flexible scintillator can maintain close contact with the sample. For example, if the flexible scintillator is on average 0.1 mm from the surface, then the rigid scintillator becomes less favorable for a line source at 0.45 mm as seen in Figure 7. The signal point source would fall off proportional to d^{-2}. One of the important consequences of this is that the sensitivity to large area sources, for example the background due to healthy tissue, will drop off less with distance than the smaller focal sources of interest. This means we may expect that despite the lower specificity and sensitivity of the material, the flexible scintillator will give us better signal to background noise for clinical specimens compared with the CaF_2.

3.4 Preclinical mouse model results

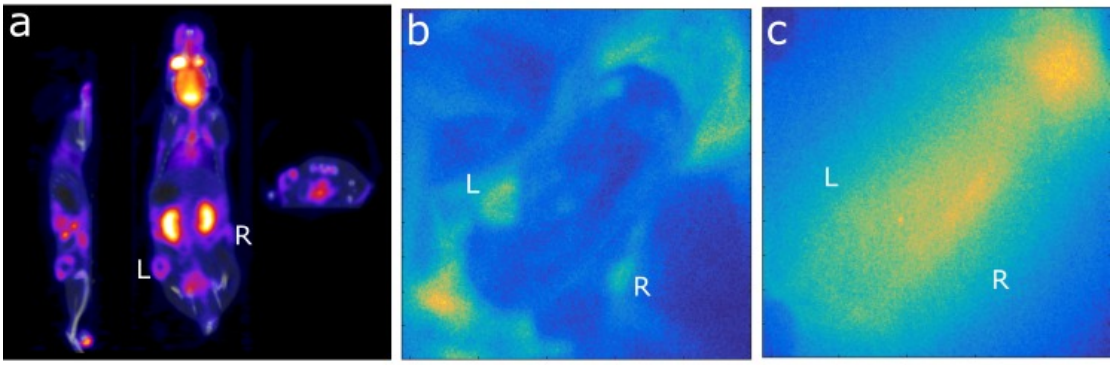

Figure 8. Images obtained from mouse 3. The positions on the planar images where the left and right tumors should be are marked L and R respectively. a) Whole body in vivo PET/CT cross-sections taken through the left tumor. The tumor appears as a ring due to low FDG uptake in the necrotic center. b) Autoradiography image taken with the flexible scintillator from above with the mouse positioned prone on the in the 'Whole body PET-CT position'. c) Autoradiography image taken as in (b) but replacing the flexible with the rigid CaF2 scintillator. It can be seen that the tumors are no longer visible over the whole-body background.

Figure 8 shows PET and autoradiography images for Mouse 3. Internal organs with high uptake, such as the kidneys and brain show up brightest on the PET scan (8a), whilst the surface weighted autoradiography measurement with the flexible scintillator show the superficial tumors more clearly (8b). For the left tumor the mean tumor signal to noise in the healthy tissue background was 26, the SNR_{max} was 46 (based on the most intense pixel of the tumor). The other sources visible in this autoradiography image are urine and the head of the mouse. With the mouse in this position the tumors are not visible with the rigid CaF_2 (8c) or BC400 scintillators but are masked by the whole-body background.

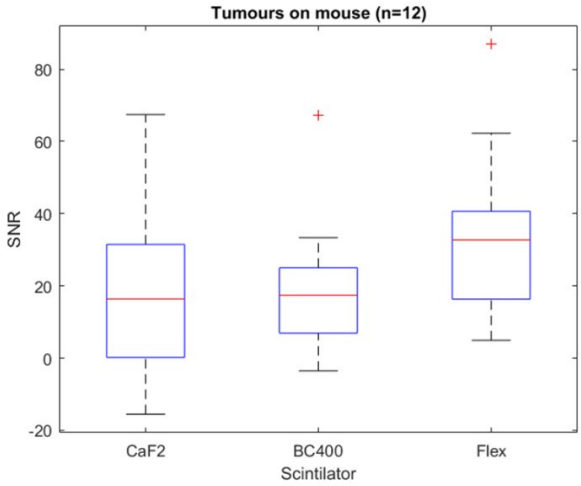

Figure 9. Box plots showing the distribution of mean tumor signal to noise in the healthy tissue background when measured with the animal on its flank. These are the collated results for all six mice for which these measurements were made. In each case both the left and right tumors were measured by imaging the corresponding flanks.

With the animal on its flank, as per the whole-body left and whole-body right positions shown in Figure 4, it was possible to obtain images of the tumors with both the rigid and flexible scintillators. It was found that the flexible scintillator could detect every tumor unlike the CaF_2 and BC400, and outperformed both in SNR as shown in Figure 9. The rigid scintillators greater sensitivity was only an advantage when measuring the excised tumors where SNR was measured against an empty background (camera noise). This is consistent with the geometry based advantages of the flexible scintillator that were investigated in the lab.

4. CONCLUSIONS

We found that the CaF_2 and BC400, respectively offered significantly better sensitivity and ^{18}F beta to Tc^{99m} specificity than the flexible scintillator when measured using a fixed geometry. However, due to the geometric advantage of conforming to the specimen, the flexible scintillator was predicted to offer better source signal to volume background noise ratios for real specimens such as wide local excisions and, equivalently, better tumor signal to whole-body background noise for a mouse model. The initial results from our preclinical mouse model work confirm this and we find the SNR to be greater than 20 with the flexible scintillator for most of the tumors measured against whole body background. We found that a resolution of 1.5 mm was achievable with a scattering background and we estimate the minimum detectable activity concentration to be 0.9 kBq/ml for 1 mm image-space sized binned pixels and a 300 s acquisition time with a EMCCD camera and f/0.95 lens. The sensitivity of the technique means it is suitable for clinical translation [19].

5. ACKNOWLEDGEMENTS

Dr. Julie Foster for animal handling and PET/CT acquisitions. Dr. Jane Sosabowski for making the preclinical imaging facility available for this study. The authors acknowledge funding from the EPSRC to support this work (EP/N022750/1).

REFERENCES

[1] Grootendorst, M. R., Cariati, M., Pinder, S., Kothari, A., Douek, M., Kovacs, T., Hamed, H, Pawa, A., Nimmo, F., Owen, J., Ramalingam, V., Sethi, S., Mistry, S., Vyas, K., Tuch, D., Britten, A., Van Hemelrijck, M., Cook, G., Sibley-Allen, C., Allen, S. and Purushotham, A., "Intraoperative Assessment of Tumor Resection Margins in Breast-Conserving Surgery using 18F-FDG Cerenkov Luminescence Imaging – A First-in-Human Feasibility Study," J. Nucl. Med. 58(6), 891-898 (2017).

[2] Poh, C. F., Zhang, L., Anderson, D. W., Durham, J. S., Williams, P. M., Priddy, R. W., Berean, K. W., Ng, S., Tseng, O. L., MacAulay, C. and Rosin, M. P., " Fluorescence visualization detection of field alterations in tumor margins of oral cancer patients," Clin. Cancer Res. 12(22), 6716-6722 (2006).

[3] Laniecea, P., Charona, Y., Cardonab, L., Pinota, L., Maitrejeanc, S., Mastrippolitoa, R., Sandkampc, B. and Valentina, L., "A new high resolution radioimager for the quantitative analysis of radiolabelled molecules in tissue section," J. Neurosci. Methods 86(1), 1-5 (1998).

[4] Duncan, K., "Radiopharmaceuticals in PET Imaging," J. Nucl. Med. Technol., 26(4), 228-234 (1998)

[5] NIST, "ESTAR stopping-power and range tables for electrons," <https://physics.nist.gov/PhysRefData/Star/Text/ESTAR.html> (2018)

[6] CERN, "GEANT 4, " <http://geant4.cern.ch/> (2018)

[7] MathWorks, "MATLAB," <https://uk.mathworks.com/products/matlab.html> (2018)

[8] Lightpoint Medical Ltd., "LightPath™ Imaging System technical specifications," Lightpoint Medical Ltd. <http://www.lightpointmedical.com/wp-content/uploads/2017/04/LightPath-technical-specifications-v1.3.pdf> (2018).

[9] Andor Technology Ltd., "Electron Multiplying CCD Cameras,", <http://www.andor.com/learning-academy/electron-multiplying-ccd-cameras-the-technology-behind-emccds> (2018)

[10] Stomper, P. C., D'Souza, D. J., DiNitto, P. A. and Arredondo, M. A., "Analysis of Parenchymal Density on Mammograms in 1353 Women 25-l9 Years Old," Am. J. Roentgenol 167, 1261-1265 (1996)

[11] Sanchez-Crespo, A., Andreo, P. and Larsson, S. A., "Positron flight in human tissues and its influence on PET image spatial resolution," Eur. J. Nucl. Med. Mol. Imaging 31(1), 44-51 (2004).

[12] Schnabel, F., Boolbol, S. K., Gittleman, M., Karni, T., Tafra, L., Feldman, S., Karlan, S., Holmes, D., Willey, S. C., Carmon, M., Fernandez, K., Akbari, S., Harness, J., Guerra, L., Frazier, T., Lane, K., Simmons, R. M., Estabrook, A. and Allweis, T., "A Randomized Prospective Study of Lumpectomy Margin Assessment with Use of MarginProbe in Patients with Nonpalpable Breast Malignancies," Ann. Surg. Oncol. 21(5), 1589–1595 (2014).

[13] Chagpar, A. B., Killelea, B. K., Tsangaris, T. N., Butler, M., Stavris, K., Li, F., Yao, X., Bossuyt, V., Harigopal, M., Lannin, D. R., Pusztai, L. and Horowitz, N. R. "A Randomized, Controlled Trial of Cavity Shave Margins in Breast Cancer," N. Engl. J. Med. 373, 503-510 (2015).

[14] Sanchez-Crespo, A., "Comparison of Gallium-68 and Fluorine-18 imaging characteristics in positron emission tomography," Appl. Radiat. Isot. 76, 55-62 (2013).

[15] Calvert, N., Tuch, D., Helo, Y., Arridge, A. and Stoyanov, D., "A Simulation Study of Spectral Cerenkov Luminescence Imaging for Tumour Margin Estimation," SPIE Med. Imag. Proc. SPIE 10137. (2017).

[16] Charles River, "Athymic nude mouse," Charles River <https://www.criver.com/products-services/find-model/athymic-nude-mouse?region=367> (2018).

[17] ATCC, "MDA-MB-231 (ATCC HTB-26™)," <https://www.lgcstandards-atcc.org/Products/All/HTB-26.aspx?geo_country=gb> (2016).

[18] Tong, S., Alessio, A. M., and Kinahan, P. E., "Image reconstruction for PET/CT scanners: past achievements and future challenges," Imaging Med. 2(5), 529–545 (2010).

[19] Mavi, A., Urhan, M., Yu, J.Q., Zhuang, H., Houseni, M., Cermik, T. F., Thiruvenkatasamy, D., Czerniecki, B., Schnall, M., Alavi, A., "Dual Time Point 18F-FDG PET Imaging Detects Breast Cancer with High Sensitivity and Correlates Well with Histologic Subtypes," J. Nucl. Med. 47(9), 1440-1446 (2006).